

## Supporting information

### **Stoichiometrically Optimized $e_g$ Orbital Occupancy of Ni-Co Oxide Catalysts for Li-Air Batteries**

Shadeepa Karunaratne<sup>a</sup>, Yasun Y. Kannangara<sup>b</sup>, Chirag R. Ratwani<sup>a</sup>, Chanaka Sandaruwan<sup>b</sup>, W.P.S.L. Wijesinghe<sup>b</sup>, Ali Reza Kamali<sup>c,d</sup>, Amr M. Abdelkader<sup>a†</sup>

<sup>a</sup> Faculty of Science and Technology, Bournemouth University, Talbot Campus, Poole, BH12 5BB, UK

<sup>b</sup> Sri Lanka Institute of Nanotechnology, Pitipana, Homagama, Sri Lanka

<sup>c</sup> School of Metallurgy, Northeastern University, Shenyang, 110819, China

<sup>d</sup> Department of Materials Science and Metallurgy, University of Cambridge, Cambridge

† Corresponding authors: Dr Amr M. Abdelkader ([aabdelkader@bournemouth.ac.uk](mailto:aabdelkader@bournemouth.ac.uk))

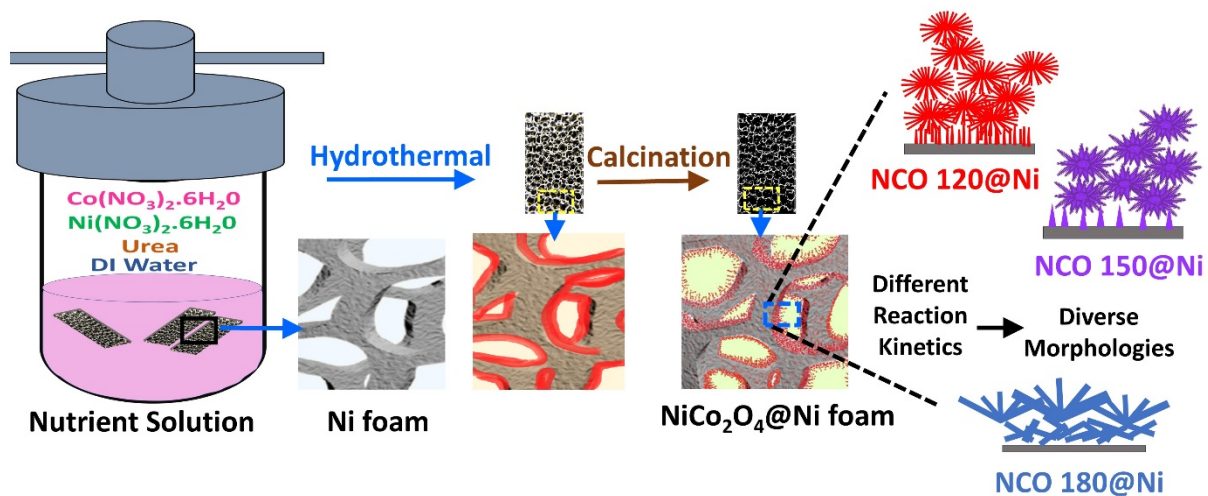


Fig S1: Schematic illustration of the growth of different Ni-Co oxide morphologies on Ni foam under different reaction environments

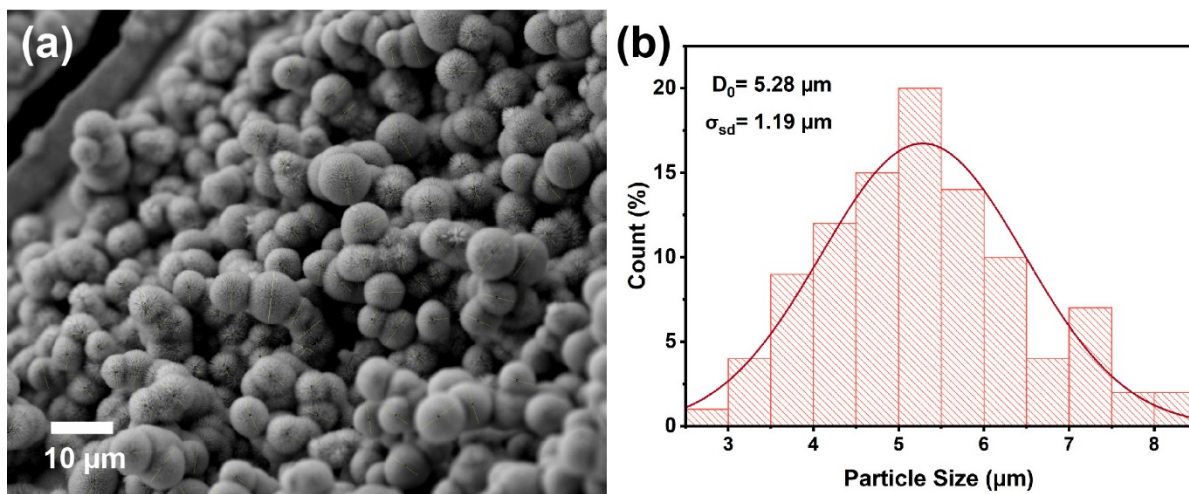


Fig S2: particle size distribution of NCO 120 catalyst

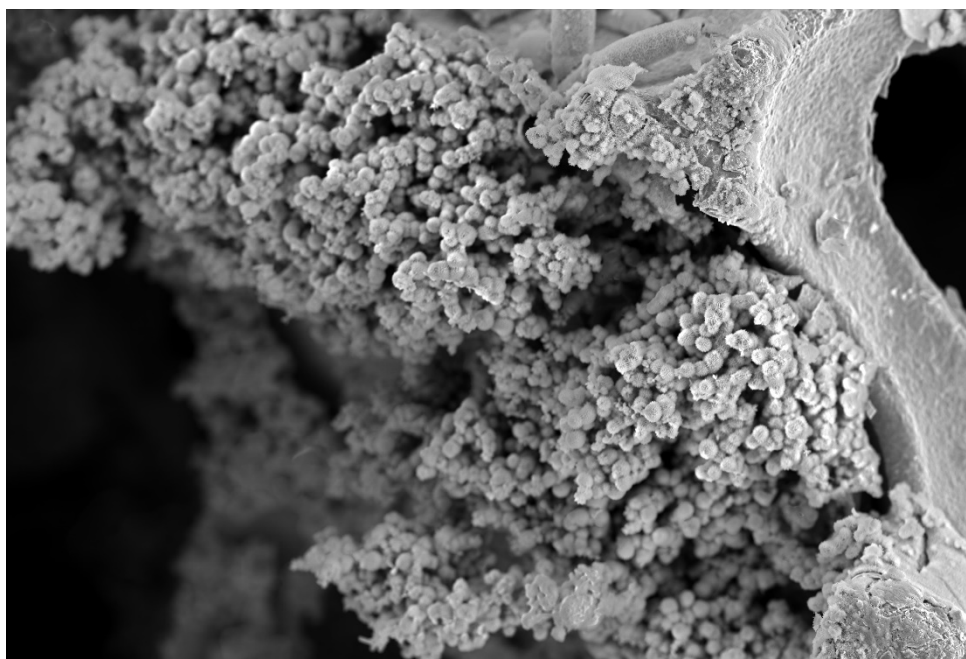


Figure S3: SEM image of NCO 150

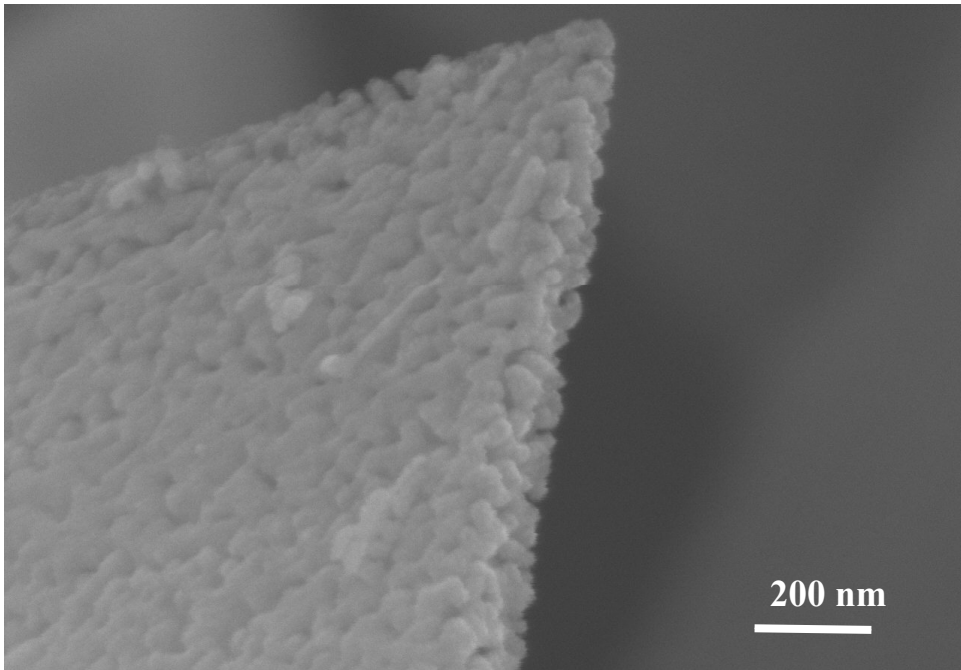


Figure S4: SEM image of NCO 180

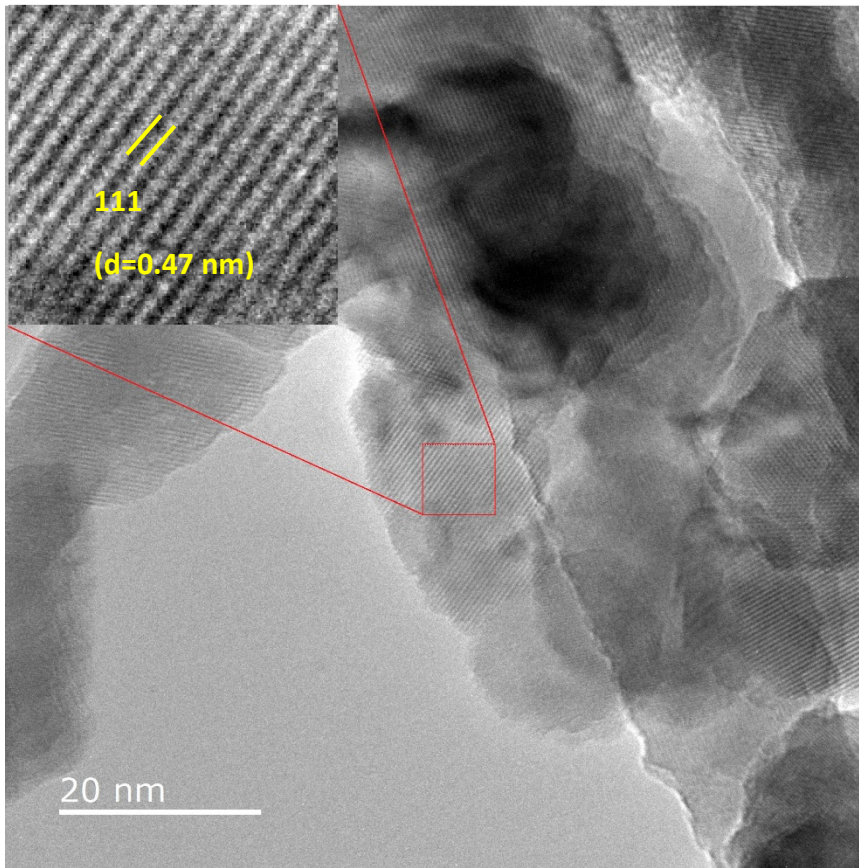


Figure S5: HR-TEM image of NCO150

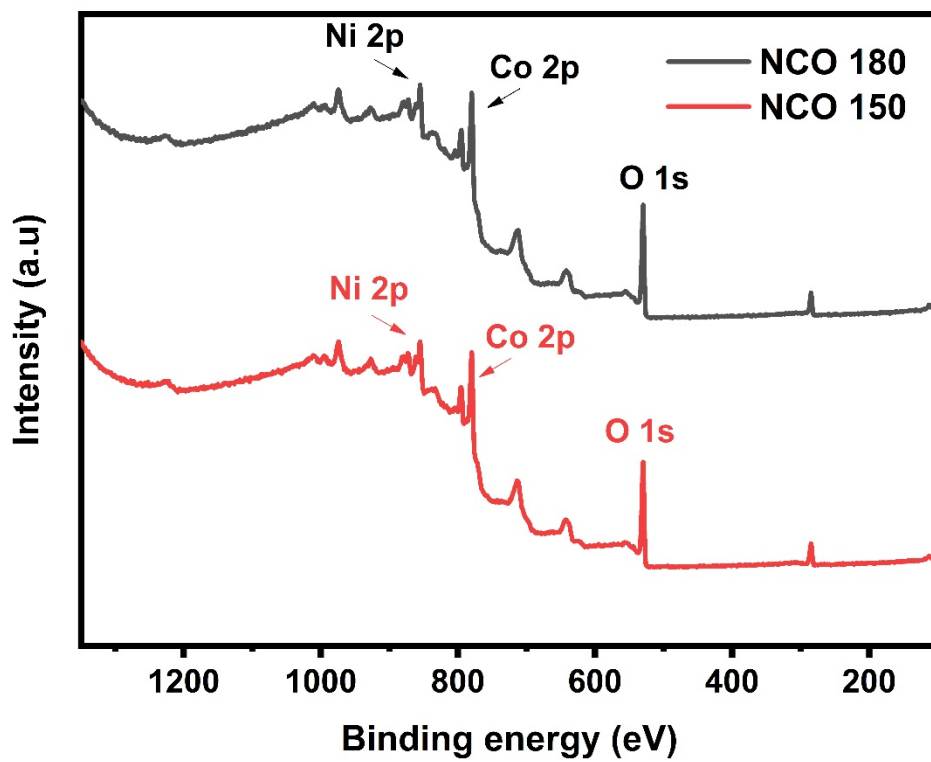


Fig S6: XPS survey scans for NCO 150 and NCO 180

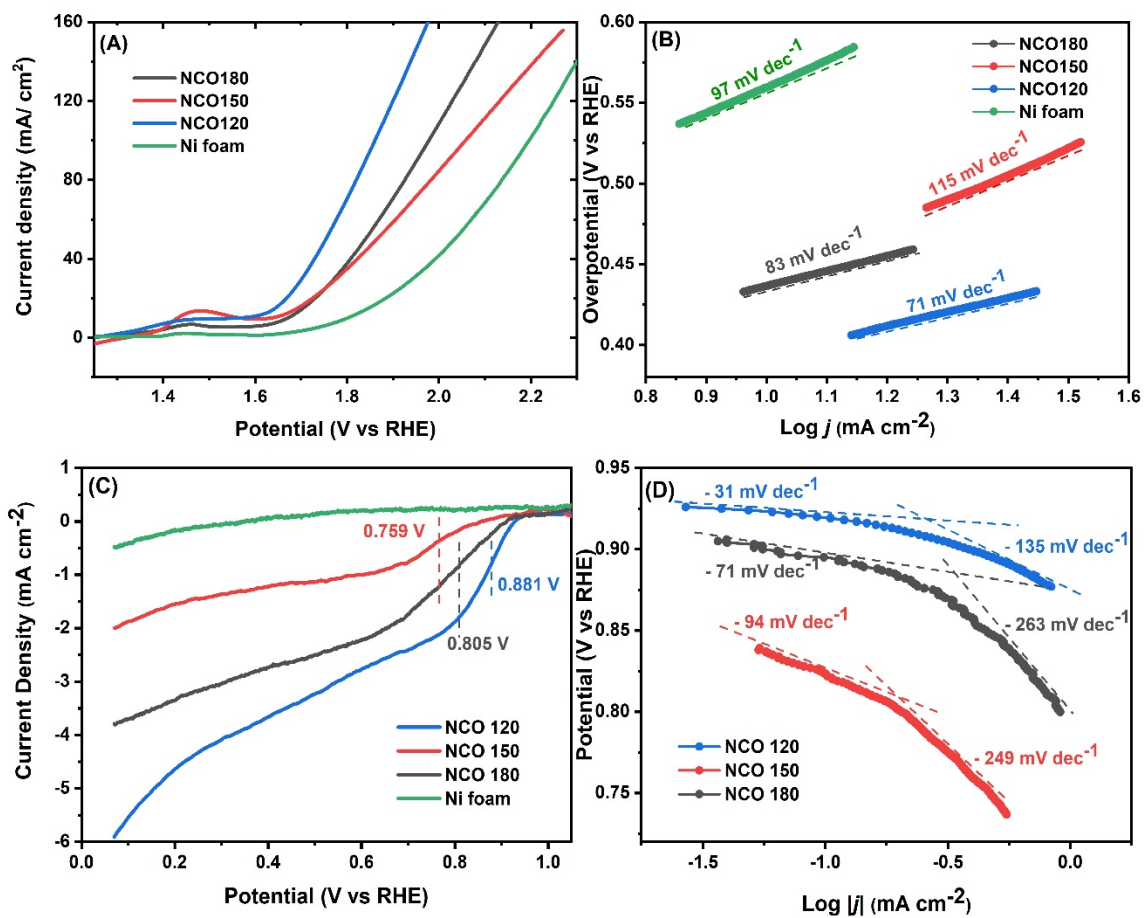


Figure S7: (A) Linear sweep voltammetric curves of NCO 120; NCO 150 and NCO 180 for OER in 0.1M KOH at a scan rate of 5 mV s<sup>-1</sup>, and (B) respective Tafel slopes, (C) ORR polarisation curves at O<sub>2</sub> saturated 0.1M KOH at a scan rate of 5 mV s<sup>-1</sup>, and (D) respective Tafel slopes

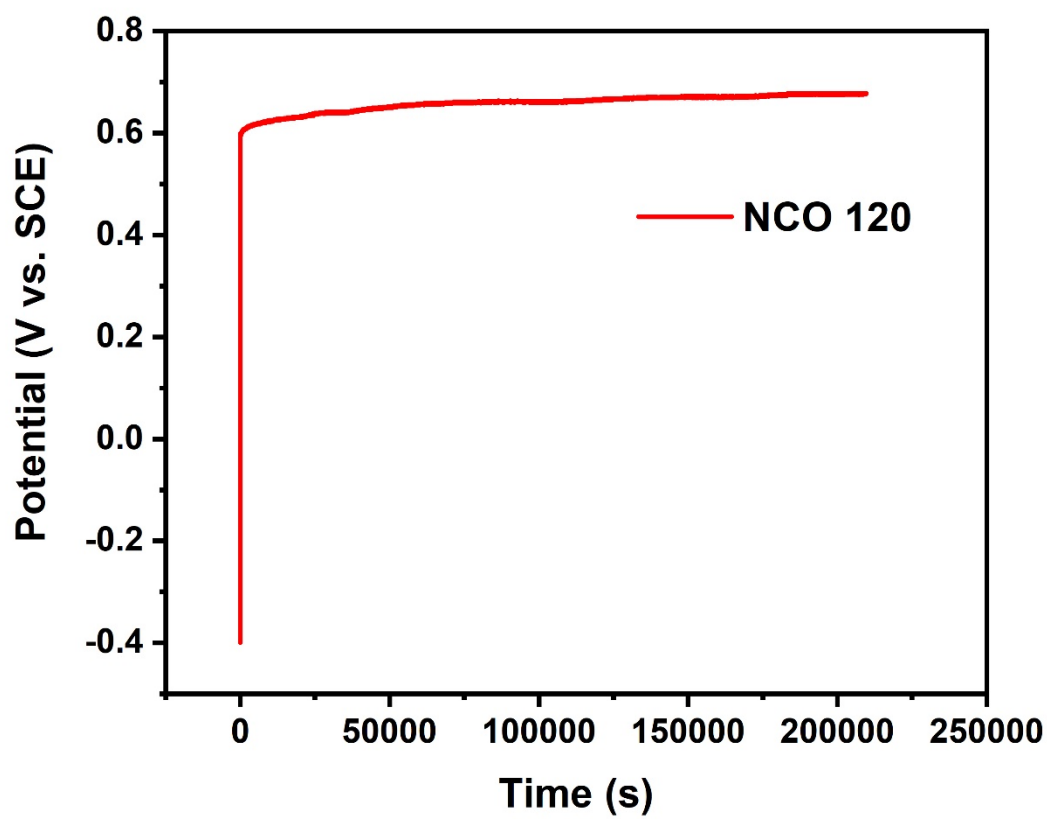


Fig S8: Galvanostatic Chronopotentiometry at current density of  $10 \text{ mAg}^{-1}$  for NCO 120

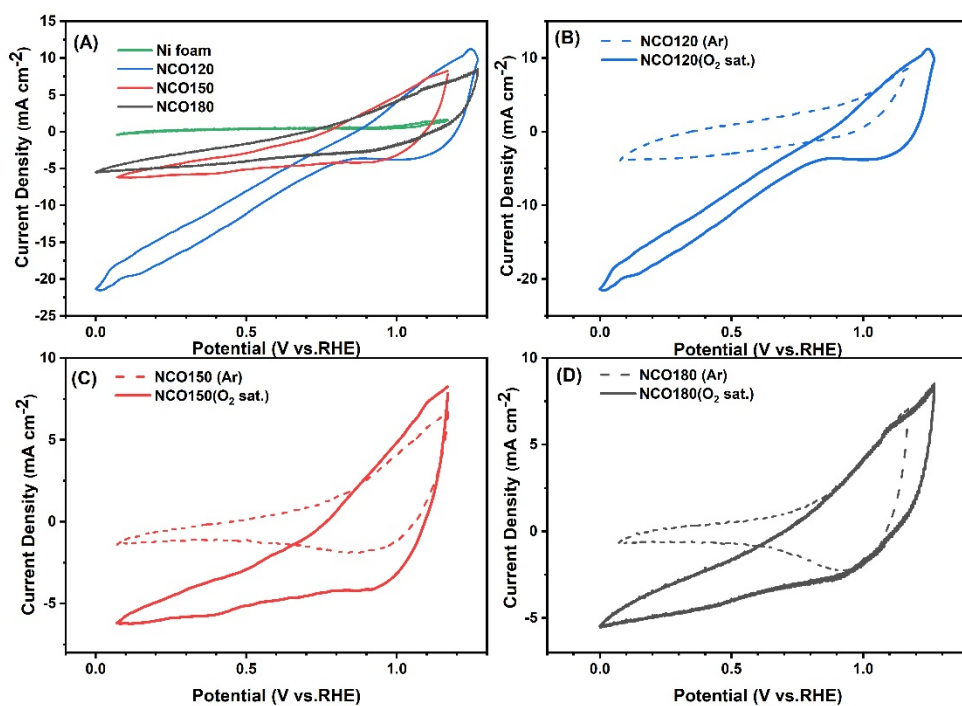


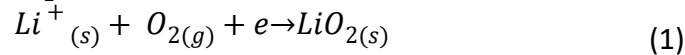
Figure S9: ORR CV for NCO 120, NCO 150, and NCO 180 under Ar- saturated and O<sub>2</sub>-saturated environments

## ORR Performance Analysis

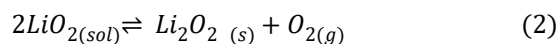
The ORR performance of NCO 120 also outperforms many other reported catalysts in the literature<sup>1,2</sup>. It is even higher than the commercial Pt/C catalyst, which was reported to have 0.89 V, 0.836 V, and 0.38 mA cm<sup>-2</sup> of ORR onset potential, halfwave potential, and the current density at 0.9V, respectively.<sup>3</sup> The Tafel plots in Figure S7 (d) show a two-step gradient. The smaller gradient at lower current densities closer to the equilibrium is mostly kinetically driven, while the larger gradients at higher current densities are further away from the equilibrium, where the diffusion effects also contribute to the gradient of the Tafel plot.<sup>4</sup> The lowest Tafel slopes of -31 mV dec<sup>-1</sup> and 135 mV dec<sup>-1</sup> were obtained with NCO 120, at least two times smaller than NCO150 and NCO 180 catalysts. Although the ORR Tafel slopes can vary with the catalyst loading and the region of interest, it is safe to mention that NCO 120 is one of the most active ORR catalysts reported so far, where it's exposed 311 and 111 facets, allowing fast adsorption of O<sub>2</sub> into its surface, supporting fast oxygen reduction kinetics. The Pt nanoparticles, commonly believed to be amongst the best catalysts, are reported with the Tafel slopes of -65 to -82 mV dec<sup>-1</sup> at lower current densities and in -100 to -300 mV dec<sup>-1</sup> at higher current densities.<sup>5</sup> Further, NCO 120 exhibits only a 0.62 V gap between OER and ORR onset potential with lower Tafel slopes, suggesting it can serve as an efficient bifunctional catalyst, whereas NCO 150 and NCO 180 exhibited larger potential gaps of 0.75 V and 0.77V.

### Cyclic voltametric result analysis

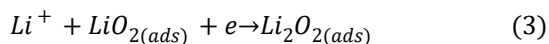
The O<sub>2</sub> approaching the cathode-electrolyte interface will undergo a single electron reduction, forming superoxide radicals, and it will subsequently be coupled with Li-ion, forming LiO<sub>2</sub> as denoted in equation 1. The cathodic peak at ~ 2.2 V is associated with the mentioned reduction of O<sub>2</sub> forming LiO<sub>2</sub>.



The diffusivity of the LiO<sub>2</sub> into the electrolyte is determined by the properties of the cathode and the electrolyte, where the electrolytes with the high donor number (DN) have a higher solubility of LiO<sub>2</sub> in the electrolyte. In such scenarios, since LiO<sub>2</sub> is an unstable superoxide in the electrolyte with a small counteraction, it is quickly disproportionate, producing low-soluble insulating toroidal-shaped Li<sub>2</sub>O<sub>2</sub> as presented in equation 2, which accommodates at the pores of the cathode. It requires higher charging overpotentials to decompose Li<sub>2</sub>O<sub>2</sub> toroids upon charging since its crystalline nature, the weak coupling between the cathode surface, and the oxidation peak presented at and above 4.0V during the anodic scan is correlated with the decomposition of such bulk and dense Li<sub>2</sub>O<sub>2</sub>.<sup>6</sup>



The produced oxygen reduction intermediates as LiO<sub>2</sub> have a high tendency to stay in contact with the cathode surface on occasion at the cathode surface supporting high adsorption of O<sub>2</sub> and LiO<sub>2</sub>. In such scenarios, LiO<sub>2</sub> could undergo a second electrochemical reduction (see equation 3) in addition to the mentioned disproportionation-producing surface adsorbed amorphous Li<sub>2</sub>O<sub>2</sub>. Further, the identified crystal defects/ oxygen vacancies could stabilise LiO<sub>2</sub> on the surface without further reduction.<sup>7</sup>



The presented additional anodic peaks at 3.19 V and 3.53 V related to NCO 120 cathode suggest the decomposition of the surface adsorbed LiO<sub>2</sub> and amorphous and non-stoichiometric Li<sub>2-x</sub>O<sub>2</sub> during the battery charging, which is significantly less for NCO 180 cathode. Even though NCO 180 exhibits good bifunctional catalytic activity, the NCO 120 cathode demonstrates superior performance with more positive ORR peak positions, less positive OER peak positions, and higher current densities. As was explained, it is noteworthy to mention that the stoichiometric changes engineering a favourable surface electronic structure with plentiful unsaturated e<sub>g</sub> orbital coordinates could lead to the high adsorption in NCO 120, supporting the formation of well-adsorbed reaction intermediates allowing an easy decomposition of the discharged products which is possibly in weakly crystalline nature. The ability to decompose a higher portion of Li<sub>2</sub>O<sub>2</sub> at a lower overpotential could suppress the amount of singlet oxygen (<sup>1</sup>O<sub>2</sub>) that could be generated during the decomposition of the discharged products at higher potentials, where the singlet oxygen was identified as the main culprit causing parasitic reactions during Li-O<sub>2</sub> battery cycling.<sup>8</sup>

### Details on characteristic behaviour in potential gap, coulombic efficiency and energy efficiency in NCO 120 and NCO 180 based LABs along with cycle number

To gain more insights into the characteristic behaviour of the constructed batteries, the potential gap, coulombic efficiency, and energy efficiency of the batteries were also evaluated during the cyclability study. The NCO 120-based LAB exhibits smooth operation, where the potential gap remains mostly stable at  $\sim 1.23$  V for the first 60 cycles after the initial rise from 0.92V, and later, a gradual rise of the potential gap is observed with  $\sim 5$  mV/cycle until the terminal voltages reach the cut-off limits. The energy efficiency of the NCO 120-based LAB exhibited similar behaviour, where the initial efficiency of 74.3% was more or less gradually decreased to 52.1% as the cut-off potentials were reached. Throughout the study, NCO 120 and NCO 180 LABs maintained good cyclability by maintaining the coulombic efficiency  $>99$  %. However, a faster decay in battery performance was observed with the NCO 180-based LAB, where energy efficiency reduced faster after  $\sim 50^{\text{th}}$  cycle owing to the large potential gaps during the period.

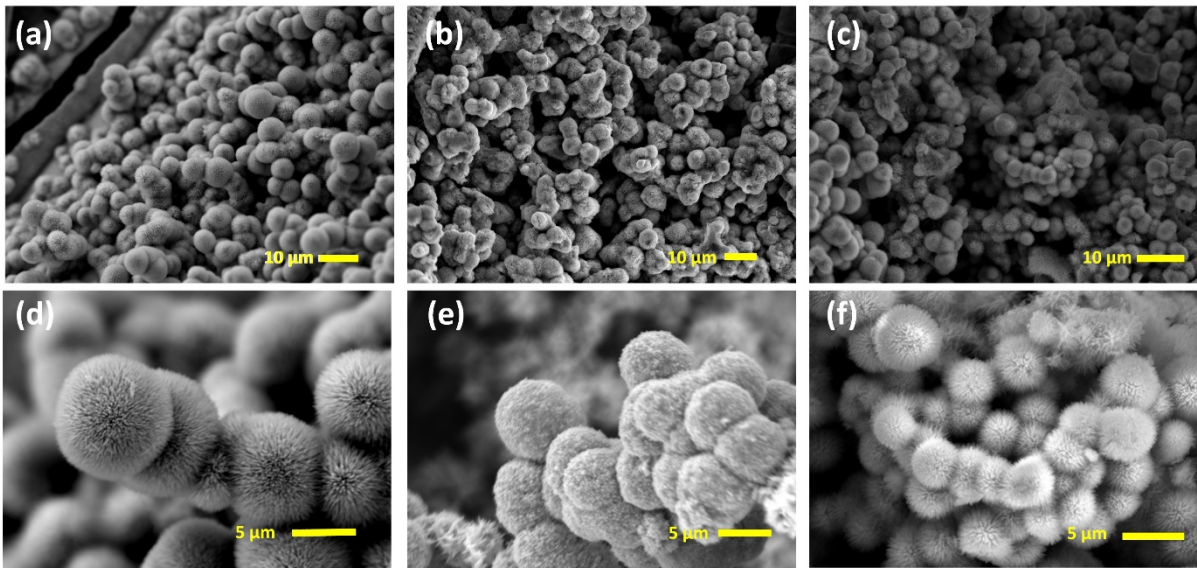


Figure S10: Ex-situ SEM analysis of the free-standing NCO 120 cathode (a, d) initially before discharge, (b, e) fully discharged, and (c, f) recharged.

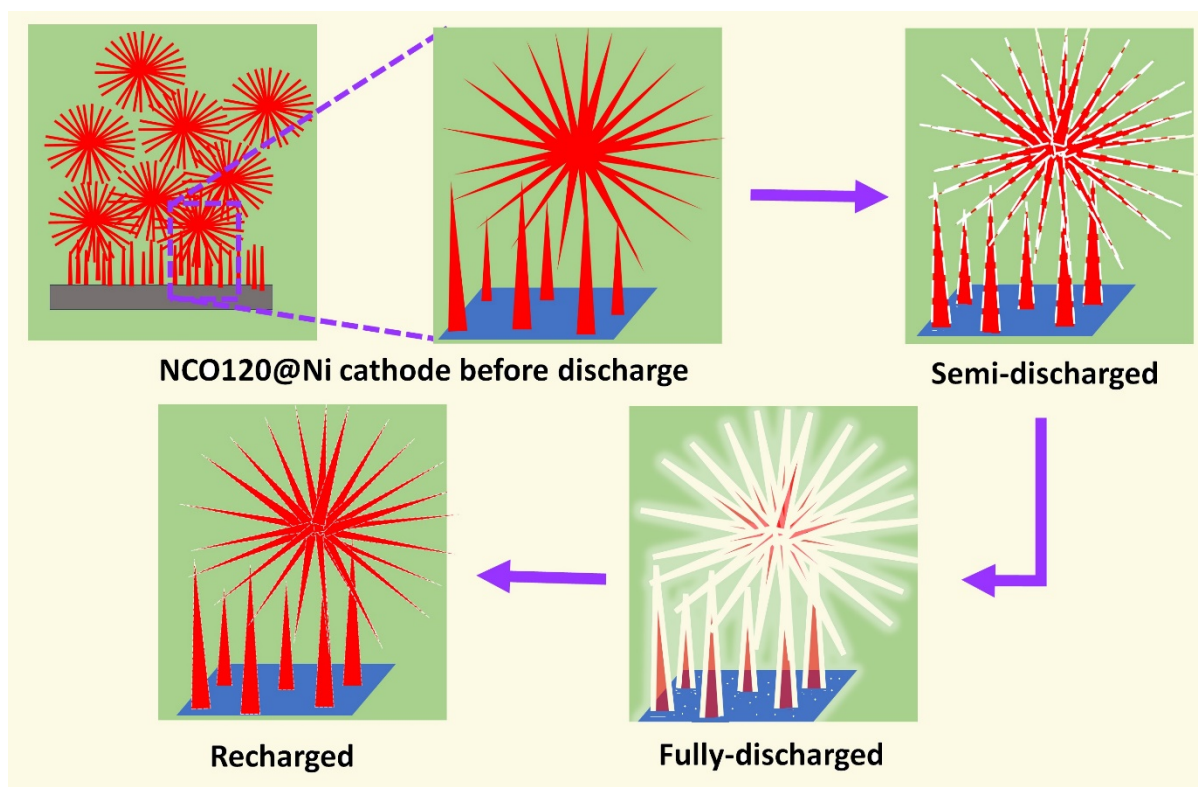


Figure S11: Schematic illustration of the surface-adsorbed growth mechanism of  $\text{Li}_2\text{O}_2$  on free-standing NCO 120 cathode during the LAB operation

## References:

- 1 W. Liu, J. Bao, L. Xu, M. Guan, Z. Wang, J. Qiu, Y. Huang, J. Xia, Y. Lei and H. Li, NiCo<sub>2</sub>O<sub>4</sub> ultrathin nanosheets with oxygen vacancies as bifunctional electrocatalysts for Zn-air battery, *Appl Surf Sci*, 2019, **478**, 552–559.
- 2 K. L. Bao, J. Y. Xu, N. F. Yu, J. B. Kuang, Z. T. Yang, H. Chen, J. L. Ye and Y. P. Wu, Oxygen Defect-Enriched Hierarchical NiCo<sub>2</sub>O<sub>4</sub> Hollow Rectangular Nanobars with Enhanced Bifunctional Oxygen Electrocatalysis for Efficient Rechargeable Zinc-Air Batteries, *Energy and Fuels*, 2022, **36**, 6542–6551.
- 3 Z. Chang, F. Yu, Z. Liu, S. Peng, M. Guan, X. Shen, S. Zhao, N. Liu, Y. Wu and Y. Chen, Co-Ni Alloy Encapsulated by N-doped Graphene as a Cathode Catalyst for Rechargeable Hybrid Li-Air Batteries, *ACS Appl Mater Interfaces*, 2020, **12**, 4366–4372.
- 4 T. Shinagawa, A. T. Garcia-Esparza and K. Takanebe, Insight on Tafel slopes from a microkinetic analysis of aqueous electrocatalysis for energy conversion, *Scientific Reports* 2015 5:1, 2015, **5**, 1–21.
- 5 L. Geniès, R. Faure and R. Durand, Electrochemical reduction of oxygen on platinum nanoparticles in alkaline media, *Electrochim Acta*, 1998, **44**, 1317–1327.
- 6 W. J. Kwak, N. Rosy, D. Sharon, C. Xia, H. Kim, L. R. Johnson, P. G. Bruce, L. F. Nazar, Y. K. Sun, A. A. Frimer, M. Noked, S. A. Freunberger and D. Aurbach, Lithium-Oxygen Batteries and Related Systems: Potential, Status, and Future, *Chem Rev*, 2020, **120**, 6626–6683.
- 7 K. L. Bao, J. Y. Xu, N. F. Yu, J. B. Kuang, Z. T. Yang, H. Chen, J. L. Ye and Y. P. Wu, Oxygen Defect-Enriched Hierarchical NiCo<sub>2</sub>O<sub>4</sub> Hollow Rectangular Nanobars with Enhanced Bifunctional Oxygen Electrocatalysis for Efficient Rechargeable Zinc-Air Batteries, *Energy and Fuels*, 2022, **36**, 6542–6551.
- 8 N. Mahne, B. Schafzahl, C. Leypold, M. Leypold, S. Grumm, A. Leitgeb, G. A. Strohmeier, M. Wilkening, O. Fontaine, D. Kramer, C. Slugovc, S. M. Borisov and S. A. Freunberger, Singlet oxygen generation as a major cause for parasitic reactions during cycling of aprotic lithium–oxygen batteries, *Nat Energy*, 2017, **2**, 17036.